Measuring the nematic order of suspensions of colloidal fd virus by x-ray diffraction and optical birefringence

Kirstin R. Purdy,[1] Zvonimir Dogic,[1] Seth Fraden,[1] Adrian Rühm,[2,*] Lawrence Lurio,[3] and Simon G. J. Mochrie[4]

[1]*Complex Fluids Group, Department of Physics, Brandeis University, Waltham, Massachusetts 02454*

[2]*Center for Material Science and Engineering, Massachusetts Institute of Technology, Cambridge, Massachusetts 02139*

[3]*Department of Physics, Northern Illinois University, DeKalb, Illinois 60115*

[4]*Department of Physics, Yale University, New Haven, Connecticut 06520*

(Received 4 October 2002; published 28 March 2003)

The orientational distribution function of the nematic phase of suspensions of the semiflexible rodlike virus fd is measured by x-ray diffraction as a function of concentration and ionic strength. X-ray diffraction from a single-domain nematic phase of fd is influenced by interparticle correlations at low angle, while only intraparticle scatter contributes at high angle. Consequently, the angular distribution of the scattered intensity arises from only the single-particle orientational distribution function at high angle but it also includes spatial and orientational correlations at low angle. Experimental measurements of the orientational distribution function from both the interparticle (structure factor) and intraparticle (form factor) scattering were made to test whether the correlations present in interparticle scatter influence the measurement of the single-particle orientational distribution function. It was found that the two types of scatter yield consistent values for the nematic order parameter. It was also found that x-ray diffraction is insensitive to the orientational distribution function's precise form, and the measured angular intensity distribution is described equally well by both Onsager's trial function and a Gaussian. At high ionic strength, the order parameter S of the nematic phase coexisting with the isotropic phase approaches theoretical predictions for long semiflexible rods $S=0.55$, but deviations from theory increase with decreasing ionic strength. The concentration dependence of the nematic order parameter also better agrees with theoretical predictions at high ionic strength indicating that electrostatic interactions have a measurable effect on the nematic order parameter. The x-ray order parameters are shown to be proportional to the measured birefringence, and the saturation birefringence of fd is determined enabling a simple, inexpensive way to measure the order parameter. Additionally, the spatial ordering of nematic fd was probed. Measurements of the nematic structure factor revealed a single large peak in contrast to nematics of rigid rods.

DOI: 10.1103/PhysRevE.67.031708 PACS number(s): 64.70.Md, 61.30.Gd, 61.30.Eb, 61.10.Eq

I. INTRODUCTION

The role of repulsive interactions in determining the phase behavior of colloidal rods was explained by Onsager in his seminal paper published in 1949 [1]. Onsager developed a free-energy theory at the second virial level describing the phase transition of both hard and charged rods from an isotropic phase in which the particles are randomly oriented to a nematic phase, in which the orientation of the particles is distributed about a preferred direction. All theoretical predictions for the properties of this phase transition, such as the coexistence concentrations and the nematic order parameter, depend on the functional form of the orientational distribution of the rods in the nematic phase [1]. Onsager chose one test function and in a later review paper Odijk showed that qualitatively similar results for the properties of the phase transition can be found by choosing a Gaussian test function [2]. The exact form of the orientational distribution function that satisfies the Onsager theory can be obtained via series expansion [3–5] or by direct iterative methods [6,7]. Determining the orientational distribution function of the nematic phase of a colloidal rod system is the most sensitive test of whether a system is described by Onsager's theory.

In this paper, we measure the concentration and ionic strength dependence of the orientational distribution function of fd virus via x-ray diffraction. The fd virus is a charged semiflexible rod with a length L to diameter D ratio $L/D \sim 130$ and a length to persistence length p ratio of $L/p = 0.4$. In the Onsager limit, the electrostatic charge on the rods can be taken into account theoretically by defining an effective diameter D_{eff}, larger than the bare diameter, which is approximately equal to the distance between particles when the interaction potential is about $k_{\mathrm{B}}T$. Details of the effective diameter calculation are outlined in Refs. [1,8,9]. An increase in ionic strength of the solution containing the charged rods produces a decrease in effective diameter. In Onsager's theory, the limit of stability of the isotropic phase is predicted to be $\pi n D_{\mathrm{eff}} L^2/4 = 4$, where n is the number density [4]. This is predicted to be valid for long rods with a length to effective diameter ratio greater than 100 [10]. Previous measurements of the isotropic and nematic coexistence concentrations of fd agree well with numerical results from Chen for $L/p = 0.4$ [8]. Theoretical models suggest that semiflexibility acts to significantly lower the nematic order parameter at coexistence. For fd, a relatively rigid polymer with p/L equal to 2.5, the nematic order parameter at coexistence is predicted to be $S=0.55$, which is significantly

*Present address: Max-Planck-Institut für Metallforschung, Heisenbergstrasse 1, D-70569 Stuttgart, Germany

smaller than that predicted for rigid rods, $S=0.79$ [11]. Several review articles describe in more detail the theoretical and experimental aspects of this and other systems described by Onsager's theory and its extensions to treat flexibility [2,10,12–18].

In x-ray diffraction, the scattered intensity consists of two parts, intraparticle scatter $F(\vec{q})$ and interparticle scatter $S(\vec{q})$. The intensity can be written as a product of the two types of scatter,

$$I(\vec{q})=NF(\vec{q})S(\vec{q},f(\vec{q})), \tag{1}$$

where $\vec{q}=4\pi\sin(\Theta/2)/\lambda$ is the three-dimensional reciprocal vector in cylindrical coordinates $\vec{q}=(q_r,q_z,\phi)$. Θ is the angle between the incident and reflected x-ray beams of wavelength λ. In a uniaxial nematic, q_r is perpendicular to the nematic director and the scattered intensity is independent of the azimuthal angle ϕ about the director. If the system is oriented such that the nematic director is in the $\hat{z}$ direction, $\vec{q}$ can be described by $\vec{q}=(q_r,q_z)$. The intraparticle interference, or form factor $F(\vec{q})$, contains information about the structure of the individual particles. $F(\vec{q})$ can also be written as $\langle f(\vec{q})^2\rangle$, where $f(\vec{q})$ is the Fourier transform of the electron density of a particle and the average is over all the particles and their orientations. The interparticle interference, or structure factor $S(\vec{q})$, contains information about the positional and orientational correlations between particles. The structure factor depends on the positions of the centers of gravity of two scatterers $\vec{R}_i,\vec{R}_j$ and their relative orientations [19]:

$$S(\vec{q})=1+\frac{1}{NF(\vec{q})}\left\langle \sum_{i\neq j}^{N} e^{i\vec{q}(\vec{R}_i-\vec{R}_j)}f_i(\vec{q})f_j(\vec{q})\right\rangle. \tag{2}$$

The orientation of the particles is included in $f(\vec{q})$ and the average $\langle\cdots\rangle$ is over all particles and their orientations. For scatterers of isotropic shape, $f_i(\vec{q})=f_j(\vec{q})$ and the structure factor and the form factor decouple, but for anisotropic scatterers, $f_i(\vec{q})\neq f_j(\vec{q})$ unless the particle orientations are the same. Therefore, in contrast to scatter from spheres, the structure factor $S(\vec{q})$ of rods cannot, in general, be decoupled from its anisotropic form factor $F(\vec{q})$.

In a nematic system, however, there is no long ranged translational order. As a result, $S(\vec{q})$ approaches unity in the limit of high $\vec{q}$, and if $S(\vec{q})=1$, the scattered intensity is due only to the intraparticle interference diffraction and $I(\vec{q})=F(\vec{q})$. In this regime, the angular distribution of the scattered intensity is a function only the single-particle orientational distribution function. Due to the crystalline internal structure of viruses such as fd and tobacco mosaic virus (TMV), x-ray diffraction produces a complex pattern of intraparticle scatter at high $\vec{q}$ which can be used to measure the single-particle orientational distribution function of the viruses [20].

At low $\vec{q}$, the scattered intensity is dominated by $S(\vec{q})$, and the angular distribution of the interparticle interference scatter is influenced by the angular and spatial correlations between neighboring rods. When intraparticle interference scattering is absent or too weak to interpret, as in thermotropic liquid crystal systems [21], or the system of lyotropic vanadium pentoxide (V_2O_5) [18], x-ray investigations of the nematic orientational distribution rely on measuring the angular distribution from interparticle interference scattering. In this case, one does not calculate the single-particle orientational distribution function, but instead the coupled fluctuations of neighboring rods; this is predicted to overestimate the value of the nematic order parameter for highly ordered samples [21,22].

In this paper, we explore the behavior of the nematic phase of fd virus investigating the concentration and ionic strength dependence of the spatial and orientational ordering measured from both interparticle and intraparticle diffraction data. We present measurements of the orientational ordering of the nematic phase in coexistence with the isotropic phase as a function of ionic strength and compare the results with the predictions for semiflexible rods. Previously, measurements of the orientational distribution function of a nematic phase have been made either from form factor scatter as in work done by Oldenbourg *et al.* on TMV [20] and work done by Groot *et al.* and Kassapidou *et al.* on persistence lengthed DNA fragments [17,23] or from structure factor scatter as in the work done by Davidson *et al.* [18]. Using fd as our model rod allows us to measure the orientational distribution function from both intraparticle scattering and interparticle interference scattering. This permits us to experimentally resolve the question of whether or not correlations between angular and spatial order present in interparticle scatter influence the measurement of the order parameter. By measuring the birefringence of each sample, we also determined the saturation birefringence of fd. This permits measurements of the order parameter to be taken using birefringence methods that involve much simpler and inexpensive techniques than x-ray diffraction.

This paper is organized in the following manner. In Sec. II, we describe the virus system and the experimental methods. In Sec. III, qualitative observations about the diffraction data are made. This is followed by a description of the analysis technique used to extract the orientational distribution function from the diffraction data in Sec. IV. Quantitative measurements of the nematic spatial ordering and orientational ordering are presented in Sec. V. This section includes first a section describing the measured spatial ordering and then sections presenting the measured orientational distribution function and the order parameter of the nematic suspensions of fd. Section VI summarizes the significant results of this paper.

II. MATERIALS AND METHODS

The physical characteristics of the bacteriophage fd are its length $L=880$ nm, diameter $D=6.6$ nm, persistence length $p=2200$ nm, and charge per unit length of around $10e^-/\text{nm}$ at pH 8.2 [15]. When in solution, fd exhibits isotropic, cho-

lesteric, and smectic phases with increasing concentration [24–27]. The fd virus was prepared using standard biological protocols found in Ref. [28] using the JM101 strain of *E. coli* as the host bacteria. The standard yield is ~50 mg of fd per liter of infected bacteria, and virus is typically grown in 10–12 liter batches. The purified virus was extensively dialyzed against a 20 mM tris-HCl buffer at *p*H 8.2 and the ionic strength was adjusted by adding NaCl.

X-ray diffraction was done at the SAXS station on beamline 8-ID at the Advanced Photon Source at Argonne National Lab. The beam flux is 2×10^{10} photons/s for a 50×50 μm beam with a photon energy of 7.664 KeV ($\lambda = 1.617$ Å). The samples were a suspension of monodisperse fd in the cholesteric phase, sealed in ~0.7 mm diameter quartz x-ray capillaries. Cholesteric samples were unwound and aligned in a 2 T permanent magnet (SAM-2 Hummingbird Instruments, Arlington, Massachusetts 02474) [29], forming a single-domain nematic phase parallel to the long axis of the capillary and the magnetic field, which we will call $\hat{z}$. The free-energy difference between the cholesteric and nematic phases is negligible, and the theory of the phase behavior of the isotropic to nematic transition can be applied equally well to the isotropic to cholesteric transition observed in fd [8]. The magnetic field does not have a significant effect on the ordering of the nematic phase [30–32]. Samples had to remain in the magnetic field for a minimum of 15 min at low concentrations and a maximum of about 8 h at the highest concentrations. The strength of the magnetic field limited the maximum concentration at which we could unwind the cholesteric phase into a monodomain nematic to about 100 mg/ml [27].

To view the liquid crystal with a polarizing microscope, samples were placed in an index matching water bath to correct optical distortions produced by the cylindrical capillary. This was done while the samples were within the magnet in order to maintain the sample as a monodomain nematic. Alignment of the nematic sample was checked with the polarizing microscope, and using a 3λ Berek compensator, its optical retardance was measured. By measuring the optical retardance R and the sample thickness within the capillary d, we can calculate the sample birefringence $\Delta n = R/d$. Birefringence is measured because it is a simple way to determine the nematic ordering of a sample as it is equal to the nematic order parameter S times a constant Δn_{sat} intrinsic to the sample material [33]. In this system, Δn_{sat} is the saturation birefringence of perfectly aligned fd, the value of which we have measured and report in Sec. V.

The magnet and sample were then mounted in a vacuum chamber such that the sample was in the beam line, and the magnetic field was perpendicular to the incoming beam. To observe the effect of charge on the nematic phase, samples were prepared at different concentrations and ionic strengths. The fd concentration was measured with a UV spectrometer by absorption at 269 nm with an absorption coefficient of 3.84 $\mathrm{cm}^2\,\mathrm{mg}^{-1}$.

When the solutions of fd were exposed to x rays for extended time, disclination lines that matched the pattern traced by the beam could be seen with a polarizing microscope. Since our samples were exposed for varied times, a series of x-ray diffraction patterns from the samples were collected with increasing x-ray exposure time to quantify sample damage and its effects on the scattering pattern. The polarizing microscope revealed sample changes after ~6 s of exposure, but the angular spread of the diffraction peaks was not affected until exposure times increased above 10 s, at which point the angular interference peak scatter broadened significantly. The effect of exposure for <10 s on the calculation of the order parameter was not measurable. Data was collected for the interparticle interference scatter by averaging ten 10 s exposures taken at different 50×50 μm sections. To observe the much less intense intraparticle scatter, the sample was continuously moved through the 50×50 μm beam allowing for a total exposure of 120 s. A single long exposure was used to image intraparticle scatter as it resulted in less noise than multiple short exposures because readout noise on the charge-coupled device (CCD) detector was higher than the dark current. Readout noise and solvent scatter were subtracted from data images during analysis, but over the q range that was analyzed, this background scatter was very uniform and could be approximated as a constant.

III. OBSERVATIONS

The two-dimensional scattered intensity of low angle interparticle and high angle intraparticle interference peaks are shown in Fig. 1 for concentrations spanning the range over which fd is nematic at 10 mM ionic strength. The angular spread of both types of scatter broadens with decreasing fd concentration or increasing ionic strength corresponding to an increase in disorientation of the rods. The low angle structure factor peak exhibits a typical ''bowtie'' pattern characteristic of interparticle interference, half of which is shown by the data in Fig. 1(a) (the other half is symmetric about the origin) [34]. The maximum of the scattering vector q_r of this intense structure factor peak is inversely proportional to the average interparticle separation, and the radial width of the peak is inversely proportional to the correlation length of the interacting rods. We note briefly that the observation of a structure factor peak in our system of fd and in other lyotropic liquid crystal systems [18,20,23] contradicts theoretical predictions by van der Schoot and co-workers which predict that the angular dispersion of nematic rods should destroy spatial order [35,36]. At larger scattering angle, the zeroth and ± first fd layer lines are visible as shown in Fig. 1(b). These intraparticle peaks are much less intense than the interparticle interference peaks and are the result of single-particle scatter arising from the helical packing of the viral proteins. The layer lines occur at intervals along the $\hat{z}$ direction proportional to the reciprocal of the axial repeat of the helical protein coat, which is 33 Å [37]. Due to discrepancy in both intensities and scattering angle between the interparticle and intraparticle scatter, we were unable to image both the high and low angle scatter simultaneously.

Due to the short ranged positional order in the nematic phase, these intraparticle interference peaks should be independent of interparticle correlations. We confirmed this hypothesis by observing that the location of the peaks does not change with concentration as do the interparticle peaks. We

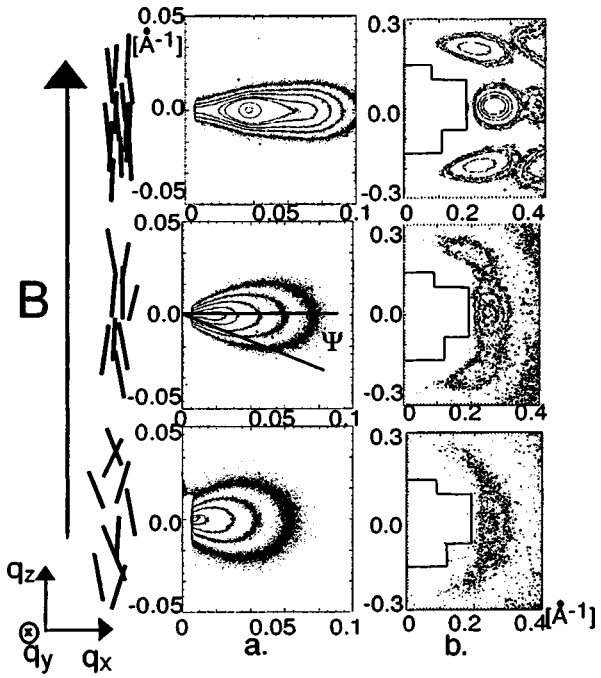

FIG. 1. Contour plots of scattering as a function of scattering vector $\vec{q}$ ($Å^{-1}$) from nematic fd due to (a) interparticle scatter and (b) intraparticle scatter; the zeroth and ± first layer lines are shown in (b). The interparticle scatter shown in (a) is hidden behind the beamstop in (b) which is located on the left side of the images. From top to bottom, the concentration of the samples are 93 mg/ml, 33 mg/ml, and 15.5 mg/ml. Samples shown are at an ionic strength of 10 mM (20 mM tris buffer) and *p*H 8.2. The magnetic field and virus orientation are perpendicular to the scatter as shown in the schematic. Ψ is the angle from the equator on the detector film. Note the scales are different in (a) and (b).

also compared our data to published fiber diffraction results for M13 [38,39]. M13 is also a filamentous bacteriophage, which differs from fd by only one amino acid per coat protein: their structures are otherwise identical and virtually indistinguishable by x-ray fiber diffraction [40]. Upon comparing published fiber diffraction data with our data from nematic fd, we observed that they were similar, but that the fiber diffraction patterns had Bragg peaks due to the hexagonal packing of the virus in the fiber, which were absent in our nematic diffraction data. We also noticed that the horizontal location of the single-particle peaks in the fiber diffraction was 4% larger than the location of our solution diffraction peaks indicating that the fiber diffraction was done on virus that had a smaller diameter than those in our nematic samples. The fibers are partially dehydrated, so it is not surprising that they become compressed. The layer line spacing, however, was not altered indicating that no stretching of the virus occurs in the fibers. From these observations, we concluded that the high angle scatter from the nematic fd was independent of interparticle correlations. Detailed analysis of both the interparticle and intraparticle diffraction continues in the following sections.

IV. ORIENTATIONAL ANALYSIS TECHNIQUE

Due to the short ranged positional order of the nematic phase, the high angle scattered intensity should be independent of interparticle correlations $S(q_r,q_z)=1$. We have demonstrated above that this is true for fd. In this case, the intraparticle scattered intensity of a system of rods is related to the orientation of those rods in the following manner [20,41]:

$$I(q_r,q_z)=\langle I_s(q_r,q_z)\rangle=\int \Phi(\Omega)I_s(q_r[\Omega],q_z[\Omega])d\Omega, \tag{3}$$

where Ω is the solid angle (θ,ϕ) a rod makes with respect to the nematic director θ and azimuthally with respect to the incident beam ϕ. Since fd is axially symmetric, $\Phi(\Omega)$ simplifies to $\Phi(\theta)$. $I_s(q_r,q_z)$ is the axially symmetric three-dimensional form factor $f(\vec{q})^2$ of a single rod. $\Phi(\theta)$ is the orientational distribution function (ODF) of the rods. Since the form of the ODF is not known exactly, three test functions were used,

$$\Phi(\theta)=\begin{cases} A\exp\left(-\dfrac{\theta^2}{2\alpha^2}\right) & (0\leqslant\theta\leqslant\pi/2) \\ A\exp\left(-\dfrac{(\pi-\theta)^2}{2\alpha^2}\right) & (\pi/2\leqslant\theta\leqslant\pi), \end{cases} \tag{4}$$

$$\Phi(\theta)=A\exp\left(-\frac{(\sin\theta)^2}{2\alpha^2}\right) \quad (0\leqslant\theta\leqslant\pi), \tag{5}$$

$$\Phi(\theta)=\frac{\alpha\cosh(\alpha\cos\theta)}{4\pi\sinh\alpha} \quad (0\leqslant\theta\leqslant\pi), \tag{6}$$

where α sets the width of each of the peaked functions, and A is the normalization constant such that $\int\Phi(\theta)\sin(\theta)d\theta d\phi=1$. Equation (6) is normalized. The first ODF is the Gaussian used by Odijk [2], the second is the function used by Oldenbourg *et al.* [20] in their study of diffraction from nematic TMV, and the third was defined by Onsager. The second moment of the orientational distribution function, or the nematic order parameter

$$S=2\pi\int_0^\pi\left(\frac{3}{2}\cos^2(\theta)-\frac{1}{2}\right)\Phi(\theta)d\cos(\theta) \tag{7}$$

was determined for the orientational distribution functions which best described the diffraction patterns.

The scatter from intraparticle interference was analyzed by comparing it to a simulated scatter created from the evaluation of Eq. (3) using a three-dimensional model for the single rod form factor and a trial ODF. Previously, Oldenbourg *et al.* measured the ODF from the intraparticle interference scatter of TMV by simplifying Eq. (3) to a one-dimensional integral at a constant q_r [20]. This one-dimensional method could not be used for intraparticle fd scatter because fd has a protein coat with a pitch much larger than that of TMV, 33 Å versus 23 Å, respectively, resulting in layer line overlap at low concentrations. Instead, the radial intensity distribution of single rod was modeled by [41]

$$I_s(q_r,q_z)=I_m(q_r,q_z)\sqrt{2\pi}\alpha q_r. \tag{8}$$

I_m are the scattered intensities along the middle of the zeroth and $\pm$ first layer lines of our most aligned nematic sample $S=0.96$ and Gaussian $\alpha=0.11$ as determined by the interparticle interference peak. The intraparticle interference data that fell on the detector in the range of $q_r=0.19$–0.33 Å^{-1}, which encompasses the lowest q_r peak on each of the three layer lines visible in the interference pattern, was fitted to the model diffraction images. For each diffraction pattern, an α was found for each trial distribution function that minimized a computed χ-squared value,

$$\chi^2=\sum_i [(I_{data_i}-B)+CI_{model_i}]^2, \tag{9}$$

where B and C are fitting parameters and i sums over the pixels in the scattered image. B was calculated once for each scattered image, and was not adjusted when comparing different ODF's. For more details of the model and analysis of the intraparticle diffraction images, refer to Appendix A.

To measure the orientational distribution function from the interparticle peak, the method of Oldenbourg *et al.* was used because the scatter consists of only one peak. In this method, Eq. (3) simplifies to a one-dimensional integral at constant q_r. This method is identical to that frequently used for analyzing thermotropic interparticle scatter, with the exception that Oldenbourg's method approximates the single rod scattering, $I_s(\Omega)$, as being proportional to $1/\sin(\omega)$ for small θ. In this equation, ω is the angle between the rod and the incident beam. This is in contrast to other analysis done on interparticle interference, in which $I_s(\Omega)=1$ [21,22,42]. The $1/\sin(\omega)$ proportionality attempts to include finite size of the rod into the calculation of the ODF. For more details, refer to Appendix A.

V. EXPERIMENTAL RESULTS AND DISCUSSION

A. Nematic spatial ordering

The location of the maximum q_m of the first interference peak and its radial width Δq_m were measured along the equator $q_z=0$ in order to obtain information about the spatial ordering of the system. Since we are only analyzing data along the equator, these properties can be determined by dividing the equatorial form factor $F(q_r,0)$ from the scattered intensity peaks $I(q_r,0)$ and then by fitting the remaining structure factor peak $S(q_r,0)$ to a Gaussian $S(q_r,0)=e^{-(q_m-q_r)^2/2(\Delta q_m)^2}$ as done in Ref. [43]. $I(q_r,0)$ and $S(q_r,0)$ are shown in Fig. 2 for three different samples. The equatorial form factor scatter was approximated by the Fourier transform of the known equatorial projection of the cylindrically averaged electron density of fd [44]. The electron density was approximated by binning the radial electron density into ten sections as illustrated in the inset of Fig. 2(a). The location of the equatorial peaks produced by the Fourier transform of the electron density agree with the equatorial form factor data obtained at higher angle, but the increase in $S(q_r,0)$ at high q_r shown in Fig. 2 indicates that this approximation is only qualitatively correct at high q_r and that the presence of background noise in the interparticle diffraction data hides any high q_r form factor information. At high concentrations, the scattered intensity is much stronger than the readout noise and as a result we are able to analyze the structure factor data to higher q_r than at low concentrations.

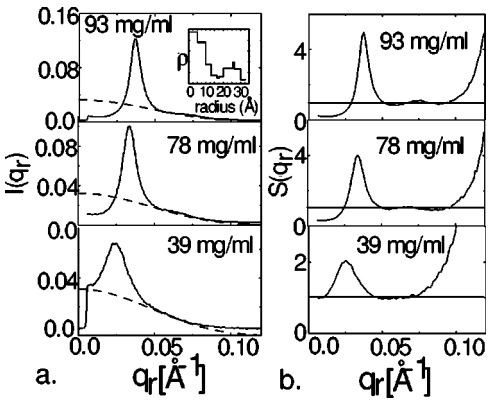

FIG. 2. (a) Equatorial intensity profile $I(q_r)$ and (b) equatorial structure factor $S(q_r)$ for three representative samples at 10 mM ionic strength and pH 8.2. The smaller inset graph is the binned cylindrically averaged electron density ρ used to calculate the equatorial form factor shown as a dashed line. The deviation of the structure factor from one at high q_r is due to both background noise in $I(q_r)$, which hides the actual form factor, and a loss of accuracy in the model form factor at high q_r.

The q_m and Δq_m measured are plotted as a function of concentration for two different ionic strengths in Fig. 3(a). With increasing concentration c, the average rod separation decreases as $c^{-1/2}$ ($q_m \propto c^{1/2}$) as expected for both isotropic and nematic suspensions of rods [19,23]. At a given concentration, the rod separation remains constant and the variance increases with decreasing ionic strength. The electrostatic repulsion present between the rods causes the rods to maintain the maximum separation possible, but a smaller effective diameter at high ionic strength allows for more fluctuations. The number of rods per correlation length $q_m/\Delta q_m$ is plotted as a function of concentration in Fig. 3(b). The concentration dependence of $q_m/\Delta q_m$ is much more significant at 10 mM ionic strength, than at 110 mM, indicating that at high ionic strength, the rods are less correlated.

It is interesting to note that the second interference peak is much weaker than the first interference peak indicating a large Debye-Waller factor. This is in contrast to charged 3D spherical and 2D disk systems which show a much stronger second, and even a third interference peak [45,46]. The structure factor of nematic fd also contrasts that of nematic end-to-end aggregated TMV, a very rigid rod, which has a structure factor closely resembling that of the 2D disk systems [43]. One way to interpret the large and sharp first peak in the structure factor of fd is that flexible nematic rods have long range spatial correlations similar to a dense fluid of disks. However, the near absence of secondary peaks in the structure factor implies that fd particles have a greater degree of positional disorder about their average position than do disks. Perhaps, the flexibility of fd accounts for this dramatic difference in spatial organization.

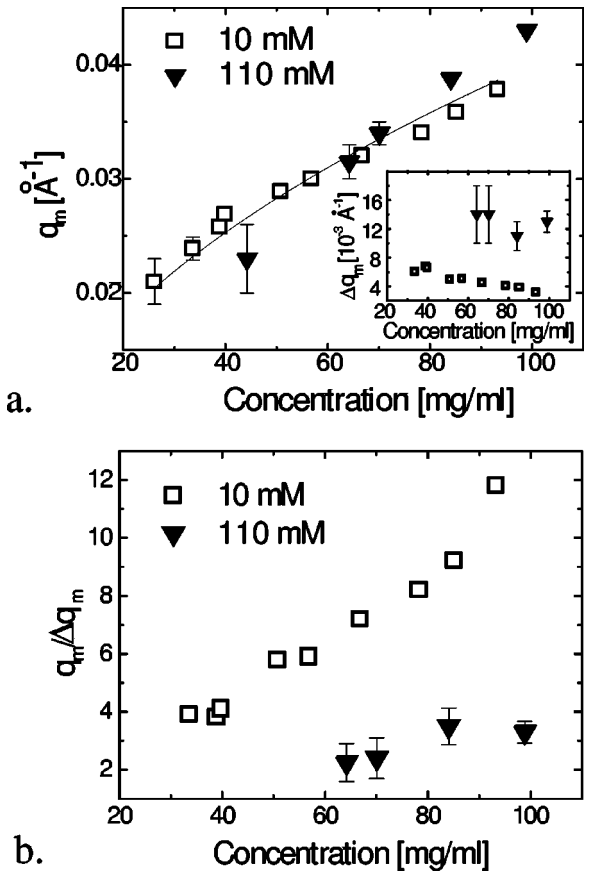

FIG. 3. (a) The concentration dependence of the maximum q_m of the interparticle interference peak. The average rod separation is a distance of $2\pi/q_m$ Å. The equation of the curve fitted to the combined data sets is $q_m = 0.004c^{1/2}$. The inset graph shows concentration dependance of the variance of the interference peaks Δq_m. (b) The concentration dependance of $q_m/\Delta q_m$, the number of rods per correlation length. Squares (□) are at 10 mM and triangles (▼) are at 110 mM ionic strength and *p*H 8.2.

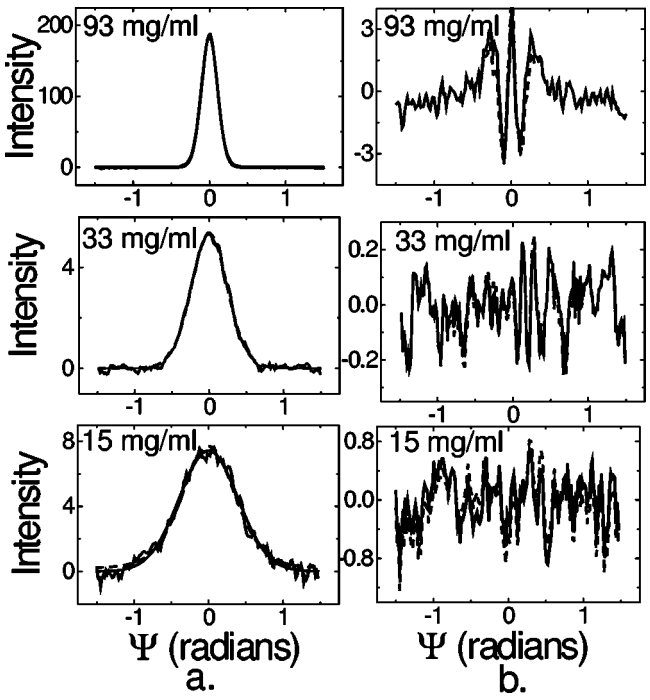

FIG. 4. (a) Angular intensity scan at $q_r = 0.07 \pm 0.001$ Å^{-1} from the three diffraction patterns shown in Fig. 1(a) with best-fit curves calculated from the three trial ODFs. The solid fit line represents the fit of both the Gaussian and Onsager ODFs, the dotted line is the fit of Oldenbourg's ODF. (b) Residue ($I_{data} - I_{fit}$) plot. Ψ is illustrated in Fig. 1(a).

B. Determining the nematic orientational distribution function

By examining the χ^2 values obtained from orientational analysis (Sec. IV) of the interparticle and intraparticle scatter, and the residues (I_{data}-I_{fit}) from the interparticle scatter orientational analysis, we determined that analysis of x-ray diffraction data does not yield a unique orientational distribution function. The Gaussian and the Onsager distribution function each fit the intensity data equally well when comparing residues and χ^2 values from each of the two functions. However, we were able to eliminate Oldenbourg's distribution function from the possible ODF forms because it did not accurately model the tails of the diffraction data at low concentration. This insensitivity of x-ray diffraction to the exact form of the ODF was predicted by Hamley who showed that x-ray patterns are insensitive to higher-order terms in the spherical harmonic expansion of the orientational distribution function and therefore only an approximation to the full orientational distribution function can be found [47].

To demonstrate this assertion, the scattered interparticle intensity at a constant radius of $q_r = 0.07 \pm 0.001$ Å^{-1} is plotted in Fig. 4(a) with the best-fit model intensities for each of the three ODFs. Ψ is the angle from the equator on the detector film as illustrated in Fig. 1(a). The actual best-fit orientational distribution functions calculated from these interparticle angular scans are shown in Fig. 5. The residues calculated from the interparticle and intraparticle interference results for the three samples are illustrated in Figs. 4(b) and 6(c), respectively. The intraparticle scatter residues shown are for the scattered intensity shown in Fig. 6(a) minus the model images shown in Fig. 6(b) created with the Gaussian ODF. The intraparticle model scatter produced relatively uniform residues indicating that it was a qualitatively good model. In two dimensions [Fig. 6(c)], we were unable to distinguish differences between residue plots of ODFs of the same width, therefore residue analysis was limited to the interparticle scatter [Fig. 4(b)].

At high concentration, small systematic disagreements between the best-fit models and the data are most visible in the residue plots in Figs. 4(b) and 6(c), but each of the three models and their respective ODFs are nearly indistinguishable. Except at low concentration, the best-fit model intensities obtained from the three distribution functions cannot be distinguished from one another both by analyzing residue plots and by comparing minimum χ^2 values computed from the fitting routine. At low concentration, the systematic disagreements between the data and the fits are lost in the noise, but disagreements in fits from different ODFs become visible. The best-fit model intensities from the Gaussian and Onsager ODFs are indistinguishable, but the residues from

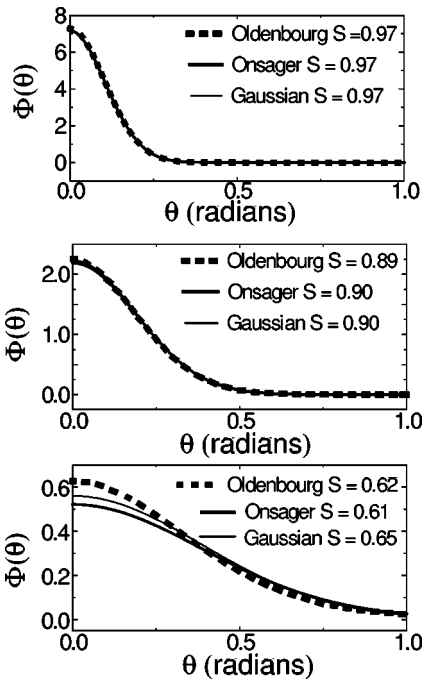

FIG. 5. Orientational distribution functions calculated from the interparticle angular intensity scan at constant radius $q_r = 0.07 \pm 0.001$ Å^{-1} shown in Fig. 4(b). Gaussian (thin solid line), Oldenbourg (dotted line), and Onsager (thick solid line) ODFs are shown. Order parameters shown are calculated from each ODF. From top to bottom, the concentrations of the samples are 93 mg/ml, 33 mg/ml, and 15.5 mg/ml. The ionic strength of the samples is 10 mM and *p*H 8.2.

the Oldenbourg ODF show disagreement, and the fits are systematically higher than the background scatter at high angle Ψ. The calculated Oldenbourg ODF also looks significantly different from the calculated Gaussian and Onsager ODFs. At the isotropic-nematic transition, the χ^2 values

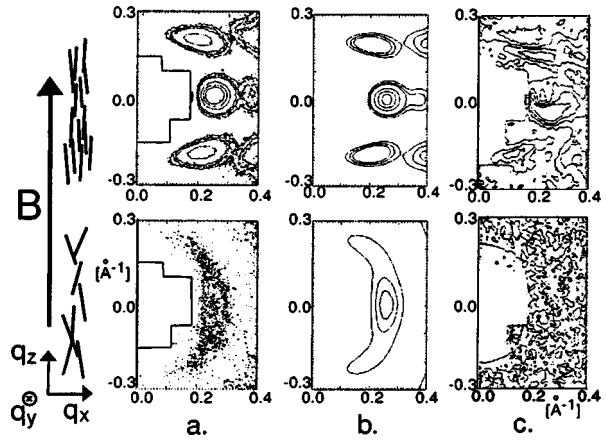

FIG. 6. (a) Contour plots from Fig. 1(b) of scattering from nematic fd samples due to intraparticle interference. Bottom scatter is at 15.5 mg/ml and top is at 93 mg/ml. Samples were at 10 mM ionic strength *p*H 8.2. (b) Simulated intraparticle scatter using a Gaussian ODF that best fit the intraparticle scatter shown in (a). (c) Residue $(I_{data} - I_{fit})/I_{fit}$ plot. Maximum residues in (c) are $\pm 10\%$. The axes of the plots are labeled in inverse angstroms.

computed from the Oldenbourg ODF were also consistently higher. From these qualitative observations, we argue that the distribution function used by Oldenbourg *et al.* does not describe our diffraction data as well as the Gaussian or the Onsager distribution function at low concentrations. The Gaussian and the Onsager orientational distribution functions fit the diffraction data equally well.

Due to small differences in the trial orientational distribution functions (as illustrated in Fig. 5), best-fit ODFs vary slightly in their width, and subsequently returned slightly different order parameters; but the order parameters calculated from the best-fit Gaussian and Onsager ODFs were in agreement with one another for a given sample within the experimental uncertainty of $\Delta S/S < 6\%$. Order parameters calculated with the Oldenbourg ODF were in common agreement at high concentrations, where the model scatter agreed with the data. The nematic order parameter calculated at multiple q_r across interparticle peak also remained relatively constant, $\Delta S/S \leqslant 4\%$. Since we cannot distinguish between the Gaussian and the Onsager model scatter, the order parameters to be presented henceforth are an average of the values calculated from only the Gaussian and the Onsager ODF, and the uncertainty on the values given are a combination of experimental error and uncertainty due to variation in order parameters from two trial ODFs.

C. Concentration and ionic strength dependence of the nematic order parameter

The concentration dependence of the nematic order parameters was measured from both the interparticle and intraparticle peaks and the resulting values are shown in Fig. 7. In Fig. 8, the order parameter of the nematic phase in coexistence with the isotropic phase is plotted for five different ionic strengths as a function of concentration. The coexistence concentrations are an increasing function of ionic strength. Our analysis shows that the order parameters calculated from the interparticle and intraparticle scatter are consistent with one another both as a function of concentration and of ionic strength indicating that correlations in the interparticle peak do not visibly change measured nematic order parameters. Figure 7(a) shows data obtained at an ionic strength of 10 mM and Fig. 7(b) shows data obtained at an ionic strength of 110 mM and *p*H 8.2. With increasing concentration, the order parameter increases until it saturates near $S = 1$, and at constant concentration, the nematic order parameter decreases with increasing ionic strength. At low concentrations, the scattered intensity is spread over a large area due to the broad orientational distribution function, which leads to a large decrease in the signal to noise ratio increasing the variation in the calculated order parameters to a maximum of $\Delta S/S \leqslant 10\%$. The solid line theoretical curves shown in Fig. 7 were computed from a scaled-particle theory that includes semiflexibility in the orientational entropy and electrostatic interactions by way of Onsager's effective diameter. This calculation is outlined in detail in Appendix B. For comparison, we also include as a dotted line the concentration dependence of the nematic order parameter from Onsager's theory for charged rigid rods at the second virial level as

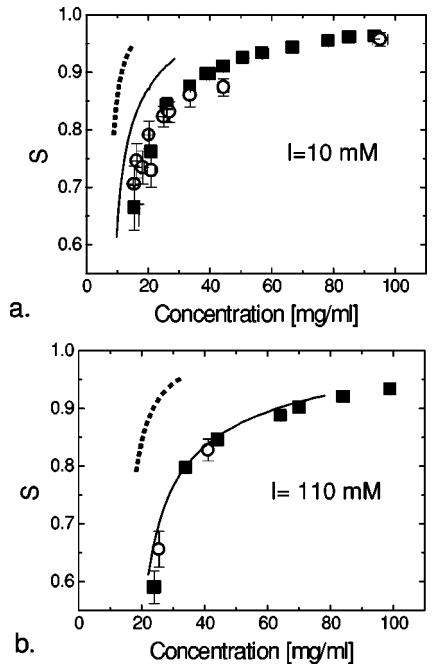

FIG. 7. Concentration dependence of the nematic order parameter. (a) is at 10 mM, and (b) is at 110 mM ionic strength and *p*H 8.2. Squares (■) are from the interparticle interference peak, and open circles (○) are results from the intraparticle peak. The solid lines shown are for a scaled-particle theory for charged semiflexible rods described in Appendix B. Dotted lines are theoretical curves for charged rigid rods in the Onsager model [7].

calculated by Lee [7]. Onsager's rigid rod theory is only valid at low concentrations near the isotropic-nematic transition, for which the second virial approximation holds, whereas the scaled-particle theory that takes into account third and all higher virial coefficients in an approximate way allows for a more adequate prediction of data at higher concentrations. The Onsager ODF was used in calculating each of these theoretical curves. The rigid rod theory does not

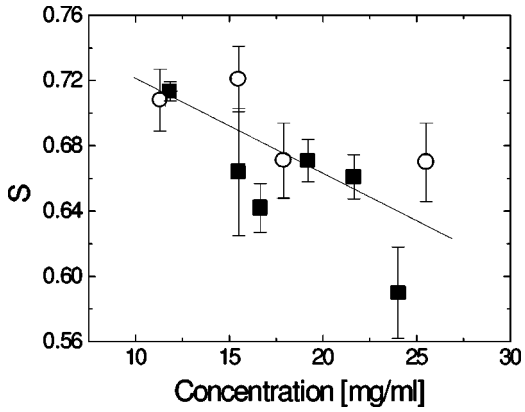

FIG. 8. Concentration dependence of the order parameter of the nematic phase coexisting with the isotropic phase as determined from the intraparticle peak (open circles ○) and the interparticle peak (solid squares ■). Increasing coexistence concentration is due to increasing ionic strength [8]. The solid line is a linear fit to the combined sets of data and is presented as a guide to the eye.

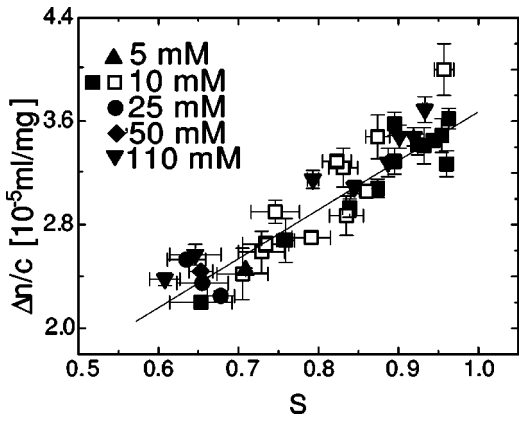

FIG. 9. Comparison of measured birefringence $\Delta n/c$ to the deduced x-ray order parameter S. Open shapes are from intraparticle interference peak measurements. Closed shapes are from interparticle interference measurements. The equation of the fitted line is $\Delta n/c = (3.8 \pm 0.3)S - (0.11 \pm 0.19)$, where $\Delta n/c$ is in units of 10^{-5} ml/mg.

agree with our data indicating that though our rods are fairly rigid, flexibility significantly changes the concentration dependence of the nematic order parameter. However, our results qualitatively agree with the scaled particle theory at low ionic strength, and quantitatively agree at high ionic strength. Deviation of the scaled particle theory from experimental results at low ionic strength is most likely due to using the effective diameter approximation to incorporate electrostatic interactions between the particles. This approximation is also valid only at low concentrations, for which the second virial approximation holds.

The order parameters calculated from the x-ray diffraction data were also compared to birefringence measurements for the whole range of concentrations and these results are plotted in Fig. 9. Birefringence was measured by the technique described in Sec. II. We expect $\Delta n/c = S\Delta n_{\mathrm{sat}}/c$, where Δn is the sample birefringence and Δn_{sat} is the birefringence of perfectly aligned fd [30,33]. We observed that the x-ray order parameter measurements of S were indeed linear with the birefringence measurements $\Delta n/c$ with a zero intercept. From this relationship, the saturation birefringence per unit concentration was measured as $\Delta n_{\mathrm{sat}}/c = 3.8 \times 10^{-5} \pm 0.3 \times 10^{-5}$ ml/mg using data from samples at five different ionic strengths. Previously, Δn_{sat} was measured by Torbet *et al.* to be $\Delta n_{\mathrm{sat}}/c = 6 \times 10^{-5}$ ml/mg. This value was calculated by assuming $S = 1$ for solutions of fd at 16 mg/ml in 10 mM tris-HCl buffer at *p*H 7.5 in a 2–4 T magnetic field [30]. At 16 mg/ml, we would expect the nematic order parameter to be $S \sim 0.75$ not $S = 1$, which would push the previously measured Δn_{sat} to a higher value even further away from our measured value. We have no explanation as to why the previously published value is inconsistent with ours.

For long rods, Onsager predicts that the nematic order parameter at coexistence remains constant, independent of ionic strength, but in Figs. 8 and 10, a weak dependence of the order parameter with ionic strength is seen. In Fig. 10, the ionic strength dependence of the nematic order parameter at coexistence is plotted as deduced from both x-ray diffrac-

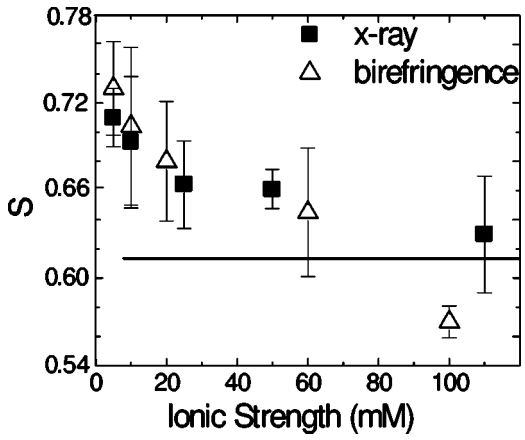

FIG. 10. Ionic strength dependence of the order parameter of the nematic phase coexisting with the isotropic phase as calculated by x-ray diffraction measurements (solid squares ■) and birefringence measurements (open triangles △). X-ray points are an average of coexistence order parameters measured from interparticle and intraparticle scatter at the same ionic strength. The solid line shows the order parameter predicted by scaled particle theory for charged semiflexible rods as in Fig. 7.

tion and birefringence measurements. The change in ionic strength from 5 mM to 110 mM corresponds to an L/D_{eff} for the rods changing from ~ 40 to ~ 85. As the effective aspect ratio approaches the long rod limit, $L/D_{\mathrm{eff}} > 100$, the coexistence order parameter decreases approaching the theoretically predicted value of $S=0.55$, as calculated by Chen for long semiflexible rods with a length to persistence length ratio, $L/p=0.4$ [11]. Even though the persistence length of fd virus is more than twice its contour length, and thus can be considered fairly rigid, all of our coexisting samples had a nematic order parameter significantly lower than the Onsager prediction of $S=0.79$ as measured by both diffraction and birefringence.

To explain the ionic strength dependence of the order parameter at the isotropic-nematic transition, we turn to electrostatic interactions. Stroobants *et al.* have shown theoretically that there is an additional electrostatic twisting factor that acts to misalign adjacent particles and decrease the nematic order parameter at coexistence [48]. This effect scales as $h=\kappa^{-1}/D_{\mathrm{eff}}$, where κ^{-1} is the Debye screening length. The effect of h on the coexistence concentrations of the system is predicted to be small [8,48] as the nematic order parameter is predicted to increase 2.4% when decreasing ionic strength from 110 mM to 5 mM, whereas we measure an increase of about 15%. Decreasing the ionic strength of the solution is also predicted to increase the nematic order parameter by the way of increasing the electrostatic persistence length [49]. However, this effect is also predicted to be small as the effective electrostatic persistence length of fd (2.203 μm at 10 mM ionic strength) is less than 1% larger than the bare persistence length (2.2 μm). Nevertheless, the observed trend of increasing order parameter with decreasing ionic strength suggests that electrostatics is significantly affecting the nematic order parameter. It is also important to note that below about 10 mM, the concentration of the virus may begin to have an effect on the ionic strength of the solution, in which the concentration of the virus counterions may act to increase the ionic strength. Overall, we expect and observe better agreement with the theoretical predictions for the nematic order parameter at high ionic strength.

VI. CONCLUSIONS

To summarize, we have observed, as predicted by Hamley [47], that the method of using x-ray diffraction to calculate the orientational distribution function is insensitive to the details of the form of distribution function used. Nevertheless, we were able to rule out the function used by Oldenbourg *et al.* [20] because we could qualitatively see that models created using this function did not fit the data equally well at low concentration and at high angle Ψ from the equator on the detector. The Onsager and Gaussian trial angular distribution functions fit the angular distribution of both the intraparticle and interparticle diffraction peaks equally well and returned similar values for the nematic order parameter. The concentration dependence of the nematic order parameter at high ionic strength, or large L/D_{eff}, as determined from both the interparticle and intraparticle scatter agrees with that predicted by a scaled particle theory of charged semiflexible rods. At low ionic strength, theoretical predictions qualitatively reproduce the concentration dependence of the order parameter. A similar agreement of the concentration dependence of nematic ordering to Onsager's theory has been measured for other semiflexible molecules [14,17,23]. This similarity demonstrates the universality of Onsager's theory and its applicability to charged semiflexible systems.

The nematic order parameters derived from both interparticle and intraparticle scatter return similar results, implying that it is sufficient to use the easier, one-dimensional analysis of the interparticle interference peak to calculate nematic order parameters as has been done for many years for thermotropic liquid crystals. It has also been shown that the relationship between the birefringence and the nematic order parameter as calculated by x-ray diffraction is linear. From this relationship, the saturation birefringence of fd was calculated. Subsequently, the order parameter can also be obtained simply by measuring the birefringence of a sample of nematic fd and rescaling it by the saturation birefringence. We note that the birefringence measurements were less reproducible than diffraction measurements as can be observed by the large variance in the data points throughout the entire range of data shown in Fig. 9.

The spatial ordering of nematic fd was also explored. The structure factor had a single large peak and a much diminished second peak in contrast to experiments with TMV, a rigid rod [43].

At high ionic strength, or large effective aspect ratio, we observed that the order parameter of the nematic phase coexisting with the isotropic phase was $S\sim 0.6$, close to the theoretically predicted value for semiflexible rods and significantly lower than the theoretical value of $S=0.79$ for rigid rods. With decreasing ionic strength, however, a weak systematic increase in the nematic coexistence order parameter was found. This is consistent with both a decrease in the

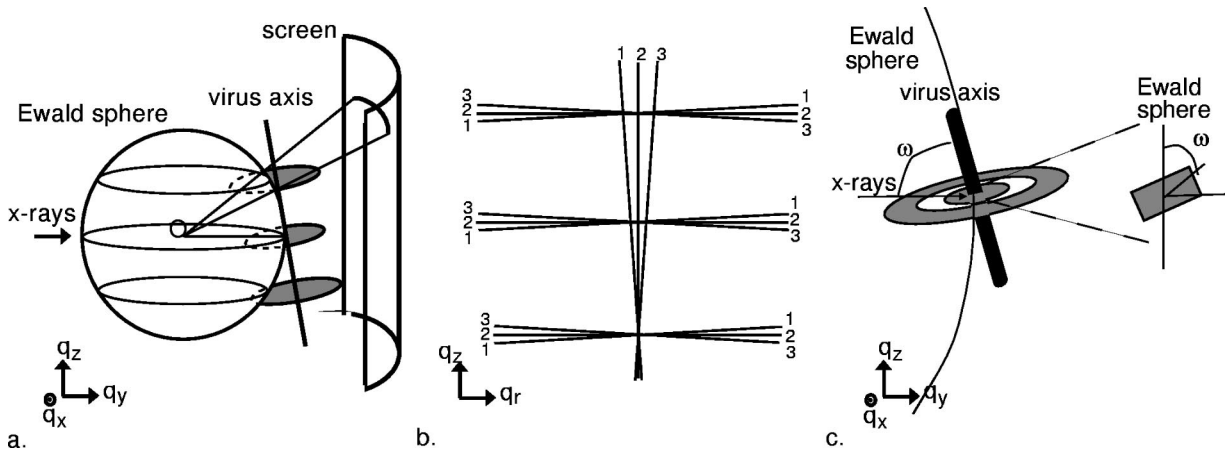

FIG. 11. (a) Schematic of the Fourier space of a single rod tilted at a slight angle. (b) Schematic showing how the intensity along the center of the layer lines decreases as q_r when there is a small amount of angular disorder. Three rod axes (vertical) are labeled 1,2,3 along with their corresponding contribution to layer lines 0,1,2 (horizontal) as shown. (c) Schematic showing the effect of the thickness of the form factor disks on the scatter with changing ω. The right hand image in (c) is an enlargement of the equatorial intersection of the Ewald sphere and I_s.

twist parameter $\kappa^{-1}/D_{\text{eff}}$ and an increase in the electrostatic persistence length, though these effects are predicted to be seven times smaller than observed. In order to fully understand the interactions that are producing the nematic phase diagrams, particularly at lower ionic strength, where L/D_{eff} is small, new theories and simulations need to be developed which include a more complete picture of the complicated electrostatic interactions.

ACKNOWLEDGMENTS

We thank E. Belamie for helping with data collection at the beam line. Work at Brandeis was supported by the NSF (Grant No. DMR-0088008). Work at Yale was supported by the NSF (Grant No. DMR-0071755). The 8-ID beam line at the Advanced Photon Source was supported by the U.S. Department of Energy (Grant No. DE-FG02-96ER45593) and NSERC. The Advanced Photon Source was supported by the U.S. Department of Energy (Grant No. W-31-109-Eng-38).

APPENDIX A: X-RAY DIFFRACTION ANGULAR ANALYSIS

If we assume that we are at sufficiently high scattering angle, where intensity variations due to interparticle interactions are negligible, then $S(q_r,q_z)=1$, and we can measure the orientational distribution function from intraparticle interference by comparing it to a simulated scatter created from the evaluation of Eq. (3). To evaluate Eq. (3), a three-dimensional model for the single rod form factor $I_s(q_r,q_z)$ was developed.

A long rod Fourier transform as a disk of thickness $2\pi/L$ oriented perpendicular to the long axis of the rod [50]. Due to the helical periodic structure along the long axis of fd, the Fourier transform of a single fd consists of a series of disks separated by a distance proportional to the reciprocal of the period [51]. This is shown schematically in Fig. 11(a). The radial intensity along these disks is a summation of Bessel functions whose exact form depends on the structure of the rod. When projected onto a screen, these disks are visible as layer lines. The images shown in Fig. 6(b) show the zeroth and $\pm$ first layer lines. For our model, the radial intensities of the disks were approximated by the scattered intensities along the middle of the zeroth and $\pm$ first layer lines I_m of our most aligned nematic sample times the radius q_r at which that intensity is located and the width α of the Gaussian ODF,

$$I_s = I_m \sqrt{2\pi}\alpha q_r . \tag{A1}$$

$\sqrt{2\pi}\alpha q_r$ is the disorientation correction term. For a small amount of disorientation of rods, the radial intensity decreases as $1/q_r$. The effect of the disorientation is illustrated in Fig. 11(b). This approximation method was developed by Holmes and Leigh, and is valid when the sample from which I_m is taken was well aligned [41]. The nematic order parameter of our most aligned sample was $S=0.96$ as measured from the interparticle interference peak.

In order to model diffraction from a nematic phase of fd, this single-particle scattered intensity is multiplied by a test ODF and integrated over all possible angles of orientation, as in Eq. (3). The intersection of the resulting three-dimensional nematic form factor and the Ewald sphere is then ''projected'' onto a two-dimensional ''screen'' and a final two-dimensional image is created, as shown in Fig. 11(a). The shell thickness of the Ewald sphere was chosen to be equal to the energy uncertainty of the experimental beam $\Delta E/E = 5 \pm 1\times10^{-4}$. The ''screen'' image is then convolved with the Gaussian point spread function of the experimental x-ray beam on the CCD camera which was approximated as $\exp[-r^2/2\sigma^2]$ with $\sigma = 0.0063$ Å^{-1}, which is slightly larger (6 pixels at 0.00105 Å^{-1}/pixel) than the photon spread quoted by the CCD camera manufacturers (4 pixels). A series of two-dimensional images were made for different orientational distribution functions with different amounts of disorder, examples can be seen in Fig. 6(b). All collected data

within the range of $q_r = 0.19$–0.33 Å^{-1} is fitted to these simulated images to find the ODF that minimized a computed χ-squared value shown in Eq. (9). This q range encompassed the innermost peak on each of the three layer lines visible in the intraparticle interference scatter.

To measure the orientational distribution function from the interparticle peak, the method of Oldenbourg *et al.* was used. Since we measure the angular spread of only one-diffraction peak, Eq. (3) simplifies to a one dimensional integral at constant q_r:

$$I(\Psi) = \int \Phi(\theta) I_s(\omega) \sin\omega \, d\omega, \tag{A2}$$

where $I(\Psi)$ is the angular intensity distribution along an arc drawn at a constant radius, Ψ is measured from the equator on the detector film, $\Phi(\theta)$ is the angular distribution function of the rods, and ω is the angle between the rod and the incoming beam. Ψ, θ, and ω are related by $\cos\theta = \cos\Psi \sin\omega$. Even though it was originally used for analyzing intraparticle scatter, this equation is identical to that used for analyzing thermotropic interparticle scatter, except that Oldenbourg's method includes a term that accounts for the length of the rod by defining the single rod scattering as $I_s(\omega) = 1/\sin\omega$ for small θ, where ω is the angle between the rod axis and the x-ray beam as illustrated in Fig. 11(c). This $1/\sin\omega$ proportionality comes from the understanding that the Fourier transform of a rod of finite length is a ring with a finite thickness, and as ω decreases, $1/\sin\omega$ increases and more of the disk intersects the Ewald sphere and is subsequently projected onto the detector screen.

Analysis done on interparticle interference from thermotropic liquid crystals typically defines $I_s(\omega) = 1$ [21,22,42]. It has been previously shown through calculations that neglecting the angular width when calculating the order parameter from interparticle interference scatter results in inaccurate values for the nematic order parameter for $S > 0.8$ [21]. However, in our analysis, we observed that changing I_s from $1/\sin\omega$ to 1 in the interparticle interference scatter analysis did not have a significant effect on the calculated value of the nematic order parameter, nor did the χ^2 values reveal any information as to which I_s better describes the data. We chose to include the effect of rod length in our interparticle scatter analysis to be consistent with our intraparticle scatter analysis, which requires a knowledge of the rod length.

APPENDIX B: SCALED PARTICLE THEORY

To compare the experimental results for the order parameter to the theory, we use the scaled particle expression for free energy of hard rods as was developed by Cotter and co-workers [52,53]. The main advantage of the scaled-particle theory is that it takes into account third and all higher virial coefficients in an approximate way and therefore should be more adequate at describing data at concentrations above the coexistence concentrations. This theory leads to a very good agreement with simulation results for the isotropic-nematic coexistence [54]. We also note that the expression for the free energy [Eq. (B1)] reduces to Onsager's second virial approximation for very long rods ($L/D \to \infty$). The free energy derived by Cotter is

$$\frac{F(\delta,\phi,\alpha)}{Nk_bT} = \ln(\phi) + \ln(1-\phi) + \sigma(\Phi(\alpha)) + \Pi_2(\delta,\alpha)\frac{\phi}{1-\phi} + \frac{1}{2}\Pi_3(\delta,\alpha)\left(\frac{\phi}{1-\phi}\right)^2, \tag{B1}$$

where ϕ is the volume fraction of rods

$$\phi = \frac{N_{rods}}{V}\left(\frac{\pi}{6}D^3 + \frac{\pi}{4}D^2L\right). \tag{B2}$$

The coefficients Π_2 and Π_3 are given by the following expressions:

$$\Pi_2(\delta,\alpha) = 3 + \frac{3(\delta-1)^2}{(3\delta-1)}\xi(\Phi(\alpha)), \tag{B3}$$

$$\Pi_3(\delta,\alpha) = \frac{12\delta(2\delta-1)}{(3\delta-1)^2} + \frac{12\delta(\delta-1)^2}{(3\delta-1)^2}\xi(\Phi(\alpha)), \tag{B4}$$

and parameter δ is the overall length over diameter ratio of the spherocylinder given by $\delta = (L+D)/D$. The functions $\xi(\alpha)$ is the excluded volume interaction between two rods as derived by Onsager,

$$\xi(\alpha) = \frac{2I_2(2\alpha)}{\sinh^2(\alpha)}, \tag{B5}$$

where I_2 is a second-order Bessel function. The expression that accounts for the rotational entropy of the rods and the entropy associated with the loss of configurations due to confinement of the bending modes of the semiflexible rods in the nematic phase has been derived by extrapolating between the hard rod and the flexible chain limits [2,55,56]. In this paper, the expression obtained by DuPré is used for numerical calculations

$$\sigma\left(\alpha, \frac{L}{p}\right) = \ln(\alpha) - 1 + \pi e^{-\alpha} + \frac{L}{6p}(\alpha - 1) + \frac{5}{12}\ln\left(\cosh\left(\frac{L}{p}\frac{\alpha-1}{5}\right)\right). \tag{B6}$$

After the expression for the free energy is obtained, we use Onsager approximation for the orientational distribution function $\Phi(\alpha)$ [Eq. (6)] and minimize the scaled particle free energy in Eq. (B1) with respect to the parameter α to find the order parameter of the nematic phase at different rod concentrations. To find out the concentrations of rods in the coexisting isotropic and nematic phases, we solve the conditions for the equality of the osmotic pressure and chemical potential.

To take into account the fact the rods are charged, instead of using the hard core diameter D in our calculations, we use

an effective diameter D_{eff} [8]. Strictly speaking, this rescaling procedure by D_{eff} is valid only for densities at which the system is described by the second virial approximation, therefore, our theoretical prediction has an uncontrolled approximation. Despite this fact, the agreement between the theory and the experiments is quite satisfactory. It is worth mentioning that there have been recent efforts to extend the validity of the scaled-particle theory to include repulsive interactions, however, this theory was not included in our calculations [57,58].

[1] L. Onsager, Ann. N.Y. Acad. Sci. **51**, 627 (1949).
[2] T. Odijk, Macromolecules **19**, 2313 (1986).
[3] G. Lasher, J. Chem. Phys. **53**, 4141 (1970).
[4] R.F. Kayser, Jr. and H.J. Raveche, Phys. Rev. A **17**, 2067 (1978).
[5] H.N.W. Lekkerkerker, P. Coulon, V. der Haegen, and R. Deblieck, J. Chem. Phys. **80**, 3427 (1984).
[6] J. Herzfeld, A.E. Berger, and J.W. Wingate, Macromolecules **17**, 1718 (1984).
[7] S.D. Lee and R.B. Meyer, J. Chem. Phys. **84**, 3443 (1986).
[8] J. Tang and S. Fraden, Liq. Cryst. **19**, 459 (1995).
[9] A. Stroobants, H.N.W. Lekkerkerker, and T. Odijk, Macromolecules **19**, 2232 (1986).
[10] J.P. Straley, Mol. Cryst. Liq. Cryst. **24**, 7 (1973).
[11] Z.Y. Chen, Macromolecules **26**, 3419 (1993).
[12] W.M. Gelbart and B. Barboy, Acc. Chem. Res. **13**, 290 (1980).
[13] H.N.W. Lekkerkerker and G.J. Vroege, Philos. Trans. R. Soc. London, Ser. A **344**, 419 (1993).
[14] T. Sato and A. Teramoto, Adv. Polym. Sci. **126**, 85 (1996).
[15] S. Fraden, in *Observation, Prediction, and Simulation of Phase Transitions in Complex Fluids*, edited by M. Baus, L.F. Rull, and J.P. Ryckaert (Kluwer Academic, Dordrecht, 1995), pp. 113–164.
[16] P.A. Forsyth, S. Marcelja, D.J. Mitchell, and B.W. Ninham, Adv. Colloid Interface Sci. **9**, 37 (1978).
[17] K. Kassapidou, R.K. Heenan, W. Jesse, M.E. Kuil, and J.R.C. van der Maarel, Macromolecules **28**, 3230 (1995).
[18] P. Davidson, C. Bourgaux, P. Sergot, and L. Livage, J. Appl. Crystallogr. **30**, 727 (1997).
[19] E.E. Maier, R. Krause, M. Deggelmann, M. Hagenbuchle, R. Weber, and S. Fraden, Macromolecules **25**, 1125 (1992).
[20] R. Oldenbourg, X. Wen, R.B. Meyer, and D.L.D. Caspar, Phys. Rev. Lett. **61**, 1851 (1988).
[21] A. Leadbetter and E. Norris, Mol. Phys. **38**, 669 (1979).
[22] P. Davidson, D. Petermann, and A.M. Levelut, J. Phys. II **5**, 113 (1995).
[23] L.C.A. Groot, M.E. Kuil, J.C. Leyte, and J.R.C. van der Maarel, Liq. Cryst. **17**, 263 (1994).
[24] J. Lapointe and D.A. Marvin, Mol. Cryst. Liq. Cryst. **19**, 269 (1973).
[25] X. Wen, R.B. Meyer, and D.L.D. Caspar, Phys. Rev. Lett. **63**, 2760 (1989).
[26] Z. Dogic and S. Fraden, Phys. Rev. Lett. **78**, 2417 (1997).
[27] Z. Dogic and S. Fraden, Langmuir **16**, 7820 (2000).
[28] J. Sambrook, E. F. Fritsch, and T. Maniatis, in *Molecular Cloning: A Laboratory Manual*, 2nd ed. (Cold Spring Harbor Laboratory, Plainview, NY, 1989), Chap. 4.
[29] R. Oldenbourg and W.C. Phillips, Rev. Sci. Instrum. **57**, 2362 (1986).
[30] J. Torbet and G. Maret, Biopolymers **20**, 2657 (1981).
[31] P. G. de Gennes and J. Prost, *The Physics of Liquid Crystals*, 2nd ed. (Oxford University Press, Oxford, 1993), Chap. 3.
[32] J. Tang and S. Fraden, Phys. Rev. Lett. **71**, 3509 (1993).
[33] A. Peterlin and H.A. Stuart, Z. Phys. **112**, 1 (1939).
[34] X. Ao, X. Wen, and R.B. Meyer, Physica A **176**, 163 (1991).
[35] P. van der Schoot and T. Odijk, J. Chem. Phys. **93**, 3580 (1990).
[36] P. van der Schoot, J. Chem. Phys. **117**, 3537 (2002).
[37] L. Makowski and D.L.D. Caspar, J. Mol. Biol. **145**, 611 (1981).
[38] M.J. Glucksman, S. Bhattacharjee, and L. Makowski, J. Mol. Biol. **226**, 455 (1992).
[39] Layer line data from M13 at *p*H 2 provided by L. Makowski (private communication).
[40] S. Bhattacharjee, M.J. Glucksman, and L. Makowski, Biophys. J. **61**, 725 (1992).
[41] K.C. Holmes and J.B. Leigh, Acta Crystallogr., Sect. A: Cryst. Phys., Diffr., Theor. Gen. Crystallogr. **30**, 635 (1974).
[42] M. Deutsch, Phys. Rev. A **44**, 8264 (1991).
[43] D. Schneider and D.L.D. Caspar (unpublished).
[44] F. Jurnak and A. McPherson, *Biological Macromolecules and Assemblies* (Wiley, New York, 1984).
[45] R. Asgari, B. Davoudi, and B. Tanatar, Phys. Rev. E **64**, 041406 (2001).
[46] J. Rino and N. Studart, Mod. Phys. Lett. B **10**, 1507 (1996).
[47] I.W. Hamley, J. Chem. Phys. **95**, 9376 (1991).
[48] A. Stroobants, H.N.W. Lekkerkerker, and D. Frenkel, Phys. Rev. Lett. **57**, 1452 (1986).
[49] T. Odijk and A.C. Houwaart, J. Polym. Sci., Polym. Phys. Ed. **16**, 627 (1978).
[50] A. Guinier, *X-ray Diffraction in Crystals, Imperfect Crystals, and Amorphous Bodies* (Dover, New York, 1994).
[51] K.C. Holmes and D.M. Blow, *The Use of X-ray Diffraction in the Study of Protein and Nucleic Acid Structure* (Interscience, New York, 1966).
[52] M.A. Cotter and D.C. Wacker, Phys. Rev. A **18**, 2669 (1978).
[53] M.A. Cotter, in *The Molecular Physics of Liquid Crystals*, edited by G.R. Luckhurst and G.W. Gray (Academic Press, London, 1979), pp. 169–189.
[54] E.M. Kramer and J. Herzfeld, Phys. Rev. E **58**, 5934 (1998).
[55] R. Hentschke, Macromolecules **23**, 1192 (1990).
[56] D.P. DuPre and S. Yang, J. Chem. Phys. **94**, 7466 (1991).
[57] E.M. Kramer and J. Herzfeld, J. Chem. Phys. **110**, 8825 (1999).
[58] E.M. Kramer and J. Herzfeld, Phys. Rev. E **61**, 6872 (2000).